ACS APPLIED ELECTRONIC MATERIALS

pubs.acs.org/acsaelm Article

Metal–Semiconductor–Metal Photodetectors Based on β-MgGaO Thin Films

Tianchen Yang, Chengyun Shou, Long Xu, Jason Tran, Yanwei He, Yuan Li, Peng Wei, and Jianlin Liu*

Cite This: ACS Appl. Electron. Mater. 2023, 5, 2122–2130 Read Online

ACCESS | Metrics & More | Article Recommendations | Supporting Information

ABSTRACT: Ultrawide-bandgap (UWBG) deep-ultraviolet photodetectors have received great attention due to their versatile applications in the fields of scientific research, civilian infrastructure, military defense, etc. In this perspective, we fabricated deep-ultraviolet β-MgGaO metal–semiconductor–metal photodetectors with interdigital Pt/Au metal contacts. β-Phase MgGaO ternary alloy thin films of different Mg atomic percentages were grown using oxygen plasma-assisted molecular beam epitaxy. Ultrawide bandgaps of 5.03, 5.09, 5.15, and 5.22 eV were achieved for thin films with and without Mg^{2+} incorporation, and light transmittances of all samples were around 90% in the visible region. Raman spectra indicate that Mg^{2+} atoms have replaced the position of Ga^{3+} ions in both octahedral and tetrahedral chains. The responsivity of the detectors was investigated. The irradiation wavelength-, temperature-, and power-dependent $I-V$ curves, photocurrent spectra, and dynamics of the photocurrents were measured. This work suggests that UWBG β-MgGaO semiconductors have a potential for deep-ultraviolet photodetectors and other photonic device applications.

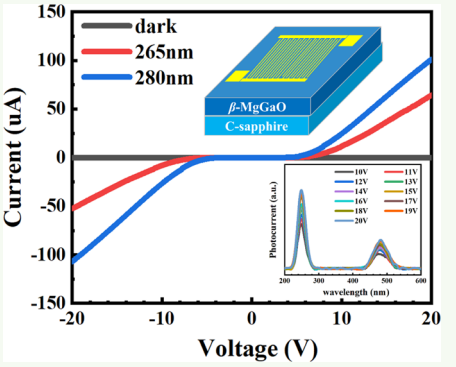

KEYWORDS: *ultrawide-bandgap semiconductors, magnesium gallium oxide, single crystal, molecular beam epitaxy, photodetector*

1. INTRODUCTION

Wide-bandgap semiconductor materials such as SiC and GaN have contributed to the development of integrated circuits, power electronics, communication and computing designs, and many novel ultraviolet (UV) optoelectronic applications.[1−5] Nowadays, ultrawide-bandgap (UWBG) semiconductor materials with a bandgap larger than ∼4 eV, such as AlN, diamond, and Ga_2O_3, have been considered as next-generation semiconductors for military and civilian applications.[5] Among these materials, Ga_2O_3 has been studied extensively recently; for example, β-phase Ga_2O_3 Schottky barrier diodes[6−8] and metal oxide semiconductor field-effect transistors[9−11] have been demonstrated to have great potential in power electronic applications. Furthermore, β-Ga_2O_3 offers promising potential to be applied in UV light detection, imaging, ozone hole monitoring, etc.[12−15] However, although n-type conductivity using the crystalline disorder method or Sn, Ge, Si, and F dopants has been demonstrated,[6,16−24] robust p-type conductivity is still very difficult to realize using Be, Li, Mg, Zn, Ca, Sr, and N dopants.[25−29] This is because the O 2p states of Ga_2O_3 make the top of the valence band very flat. A small dispersion of the valence band maximum results in a large hole effective mass and, in turn, very low hole mobility, which makes p-type conductivity impractical.[6,30] Moreover, oxygen vacancies are usually generated in these materials, which act as deep donors and compensate p-type acceptor impurities such as Zn^{2+} and Mg^{2+}. This dilemma has greatly limited the potential of Ga_2O_3 for both power electronic and optoelectronic applications.

To further enhance the performance of Ga_2O_3 radio frequency (RF) power electronic and optoelectronic devices, Ga_2O_3 heterostructures are also essential. Alternatives such as AlGaO[31−33] and ZnGaO[34,35] alloys have been reported to show great promise in terms of their bandgap tunability and compatibility with Ga_2O_3. In this work, we explore another UWBG semiconductor material, namely, magnesium gallium oxide (MgGaO). Although MgGaO amorphous films have been synthesized and reported,[36,37] β-phase MgGaO single-crystalline thin films have been rarely reported. MgGaO is promising due to the following reasons: it can be considered as a mixture of Ga_2O_3 and MgO materials, and thus its bandgap can be tuned over a wider range than that of Ga_2O_3. Moreover, the substitution of divalent Mg ions into trivalent Ga ion sites in MgGaO can significantly tune its electrical conductivity, which has the potential to achieve p-type conductivity in these UWBG semiconductors.

In this paper, MgGaO ternary alloy thin films with ultrawide bandgaps up to ∼5.22 eV were grown by plasma-assisted

Received: January 8, 2023
Accepted: March 14, 2023
Published: March 22, 2023

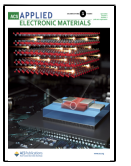

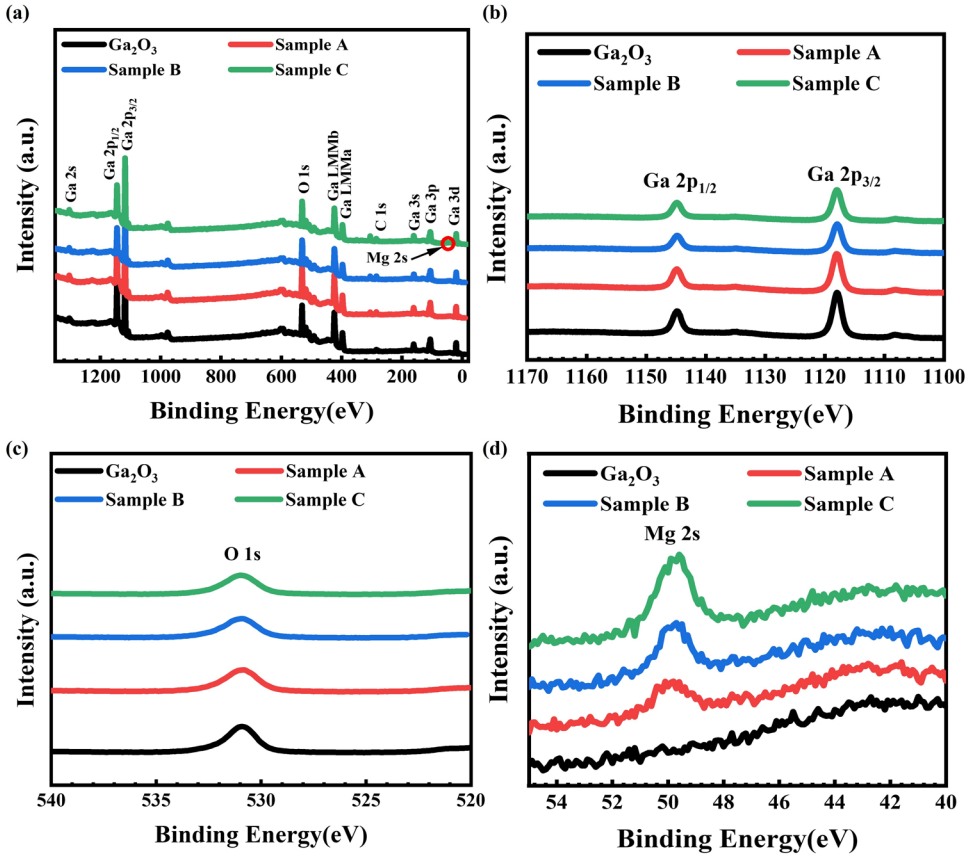

Figure 1. XPS analysis of the reference Ga_2O_3 and MgGaO samples A, B, and C: (a) survey peaks, (b) Ga 2p spectra, (c) O 1s spectra, and (d) Mg 2s spectra.

molecular beam epitaxy (MBE). Solar-blind metal−semiconductor−metal (MSM) photodetectors with good responsivity were fabricated based on MgGaO thin films with varying Mg compositions. The wavelength-, temperature-, and power-dependent $I-V$ characteristics, photocurrent spectra, and dynamics of these photodetectors were studied.

2. EXPERIMENTAL SECTION

2.1. Film Growth. β-MgGaO thin films were grown on 2 inch c-sapphire substrates using an MBE system equipped with an RF plasma-assisted oxygen source (SVT Associates Inc.). The substrates were first cleaned with isopropyl alcohol (IPA) solution (IPA/deionized water = 1:1), then with Piranha solution (H_2O_2/H_2SO_4 = 3:5) at 200 °C for 20 min, rinsed with deionized water, finally dried in nitrogen gas, and transferred to the MBE loadlock chamber immediately. High-purity elemental Mg and Ga shots (6N) (Alfa Aesar) were placed in effusion cells as the growth sources. A pregrowth annealing process was performed at a high temperature of 800 °C for 20 min to achieve an atomic-level surface within a high vacuum chamber on the order of 10^{-9} torr. During the growth of the samples, the temperature of the substrate was kept at 650 °C and an RF plasma-assisted oxygen source with a flux of 2.5 sccm was used at a power of 400 W. The temperature of the Ga cell was set to 750 °C and those of the Mg cell were set to 380, 385, and 390 °C for samples A, B and C, respectively. After 1 h growth, a post-growth annealing process was carried out at 700 °C under an oxygen atmosphere for 20 min before cooling to the room temperature. A pure Ga_2O_3 sample was grown under similar growth conditions but without Mg incorporation as a reference. The growth details of these samples are listed in Table S1 (Supporting Information).

2.2. Film Characterization. The film thickness of the samples was measured by a Filmetrics 3D Profilometer. Surface morphologies of films were characterized by a TESCAN Vega3 SBH scanning electron microscope (SEM) and a Dimension 3100 Nanoman atomic force microscope (AFM). Mg contents were measured by an energy-dispersive X-ray spectroscope (EDS) in the same SEM instrument and a Kratos AXIS Ultra DLD X-ray photoelectron spectroscope (XPS). X-ray diffraction (XRD) 2θ and omega scans of the films were measured using a Bruker D8 Advance X-ray diffractometer and Rigaku SmartLab X-ray diffractometer with Cu Kα (λ = 0.15405 nm) radiation, respectively. The phonon energies of the films were investigated by a confocal Raman microscope equipped with a high-resolution laser with a wavelength of 532 nm and a power of 60 mW (LabRAM HR, HORIBA Scientific). Room temperature ground-state absorption and transmittance spectra of the samples were obtained using a high-performance UV−Vis−NIR spectrophotometer (Cary 5000, Agilent Inc.).

2.3. MSM Photodetector Device Fabrication and Characterization. MSM photodetectors with an interdigital Pt/Au (20/100 nm) Schottky contact pattern were fabricated by standard photolithography, e-beam evaporation, and an acetone lift-off process. Optoelectronic properties of wavelength-, temperature-, and power-dependent $I-V$ characteristics, responsivity, and current−time ($I-t$) dynamics were measured using a Signatone H100 series probe station and an Agilent 4155C semiconductor parameter analyzer under the illumination of 265 and 280 nm light. Photocurrent spectra were acquired using a UV-enhanced xenon arc lamp with a monochromator set-up (Oriel Cornerstone 260, Newport Corporation).

3. RESULTS AND DISCUSSION

Samples A, B, and C have film thicknesses of ~83.1, 92.9, and 93.2 nm, respectively. Figure 1a shows XPS survey peaks of the reference Ga_2O_3, and MgGaO samples A, B, and C. (Figure 1b−d) show XPS Ga 2p, O 1s, and Mg 2p spectra, respectively. The peaks of Ga $2p_{3/2}$ and Ga $2p_{1/2}$ are located at ~1116.4 and

https://doi.org/10.1021/acsaelm.3c00035
ACS Appl. Electron. Mater. 2023, 5, 2122−2130

~1143.2 eV, respectively (Figure 1b), O 1s is located at ~543.1 eV (Figure 1c), and Mg 2p is located at ~49.78 eV (Figure 1d). Based on these peaks, the relative atomic compositions of Ga_2O_3 and MgGaO samples A, B, and C are estimated and summarized in Table 1. The Mg atomic percent of samples A, B, and C were recorded as 1.8, 3.4, and 4.0%, respectively. The EDS characterization of elemental compositions of MgGaO thin films showed values reasonably similar to the XPS data (Supporting Information, Figure S1).

Table 1. Relative Atomic Composition of Ga_2O_3 and MgGaO Samples A, B, and C

samples	Ga (atom %)	O (atom %)	Mg (atom %)
Ga_2O_3	35.6	64.4	0
A	33.8	64.4	1.8
B	28.9	67.7	3.4
C	31.1	64.9	4.0

Figure 2 shows morphological characterization results. As seen in the SEM images in Figure 2a–d, all surfaces are relatively smooth, while smoother surface are observed in MgGaO thin films with lower incorporated Mg content. The AFM 5 μm × 5 μm images are shown in Figure 2e–h, and the root mean square (RMS) roughness values are 1.29, 0.45, 0.68, and 0.80 nm for the reference Ga_2O_3 sample and MgGaO samples A, B, and C, respectively, which is in agreement with the SEM results.

Figure 3a shows the XRD pattern in the $\theta/2\theta$ scan mode of Ga_2O_3 and MgGaO samples A, B, and C. The three typical diffraction peaks located at around 19.12, 38.50, and 59.14° correspond to the β phases of $(\bar{2}01)$, $(\bar{4}02)$, and $(\bar{6}03)$, respectively, implying a clear monoclinic structure. After Mg atoms are incorporated into Ga_2O_3, all of these diffraction angles exhibit an obvious decrease as the ionic radius of Mg^{2+} ions (0.72 Å) is larger than that of Ga^{3+} ions (0.62 Å). According to Bragg's Law, the interplanar distance d will become larger and the angle of 2θ will decrease when Mg^{2+} ions replace Ga^{3+} ions.[27,38] The XRD 2θ scan data suggest that MgGaO samples A, B, and C maintain a good β phase structure. Figure S2 (Supporting Information) shows a schematic of the MgGaO monoclinic structure, assuming that two Ga atoms are replaced with two Mg atoms in the Ga_I site. Figure 3b shows the normalized XRD rocking curves of samples A, B, C and the reference Ga_2O_3 sample, respectively. The full width at half-maximum (FWHM) of the peak $(\bar{4}02)$ of β-Ga_2O_3 and samples A, B, and C were recorded at 0.0756, 0.0611, 0.0608, and 0.0565°, respectively. As the Mg composition increases, the FWHM reduces slightly but monotonically, which may be due to the lower lattice mismatch between the film and the substrate as more Mg is incorporated. Compared to the reported 1.494° FWHM of the $(\bar{2}01)$ peak of the β-Ga_2O_3 thin film,[39] it indicates a higher quality of our films.

Optical phonon modes of Ga_2O_3 and samples A, B, and C are shown in Figure 3c; four of five B_g and three of 10 A_g optical phonon-mode Raman-active peaks, namely, $B_g^{(1)\text{-}(2)}$, $B_g^{(4)\text{-}(5)}$, $A_g^{(1)}$, $A_g^{(5)}$, and $A_g^{(10)}$ modes, are observed in the MgGaO thin films. As a reference, four of five B_g and five of 10 A_g optical phonon-mode Raman-active peaks, namely, $B_g^{(1)\text{-}(3)}$, $B_g^{(5)}$, $A_g^{(1)\text{-}(3)}$, $A_g^{(5)}$, and $A_g^{(10)}$ modes, are observed in the Ga_2O_3 sample. Details of peak positions of all samples are summarized in Table S2 (Supporting Information). Compared to Raman peaks of Ga_2O_3, $A_g^{(2)\text{-}(3)}$ and $B_g^{(3)}$ modes disappear in all three MgGaO samples. In addition, the peak intensities of $A_g^{(2)\text{-}(3)}$ and $B_g^{(1)\text{-}(2)}$ modes are reduced, which implies the vibration and translation of the Ga_IO_4 tetrahedral chains after Mg^{2+} atoms are incorporated. The change of $A_g^{(5)}$ and $B_g^{(3)\text{-}(4)}$ modes indicates the deformation of $Ga_{II}O_6$ octahedral chains and the translation of the Ga_IO_4 tetrahedral chains, while the change of $A_g^{(10)}$ mode indicates the stretching and bending of the Ga_IO_4 tetrahedral chains.[40,41] Apart from the change of peak intensity, the MgGaO Raman peaks have smaller wavenumber than that of Ga_2O_3 due to larger bond lengths. The calculated average bond length for Mg–O bonds is 2.03 Å,[42] while the average Ga–O bond length for tetrahedral chains is 1.83 Å and that for octahedral chains is 2.00 Å.[43,44] The Mg–O bond length is longer than the corresponding Ga–O bonds after Mg^{2+} ions replace Ga^{3+} sites, which is due to the larger radius of Mg^{2+} (0.72 Å) than that of Ga^{2+} (0.62 Å).[45] To sum up, the difference in the Raman spectra between MgGaO

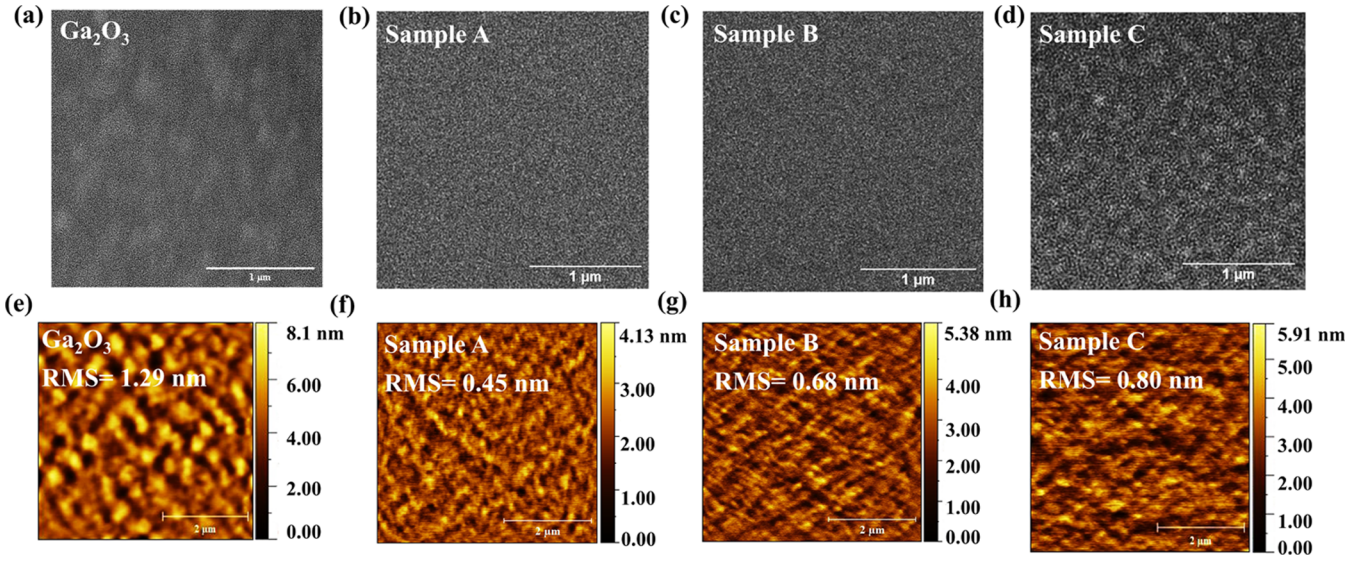

Figure 2. (a–d) SEM and (e–h) AFM images of the reference Ga_2O_3 and MgGaO samples A, B, and C, respectively.

https://doi.org/10.1021/acsaelm.3c00035
ACS Appl. Electron. Mater. 2023, 5, 2122–2130

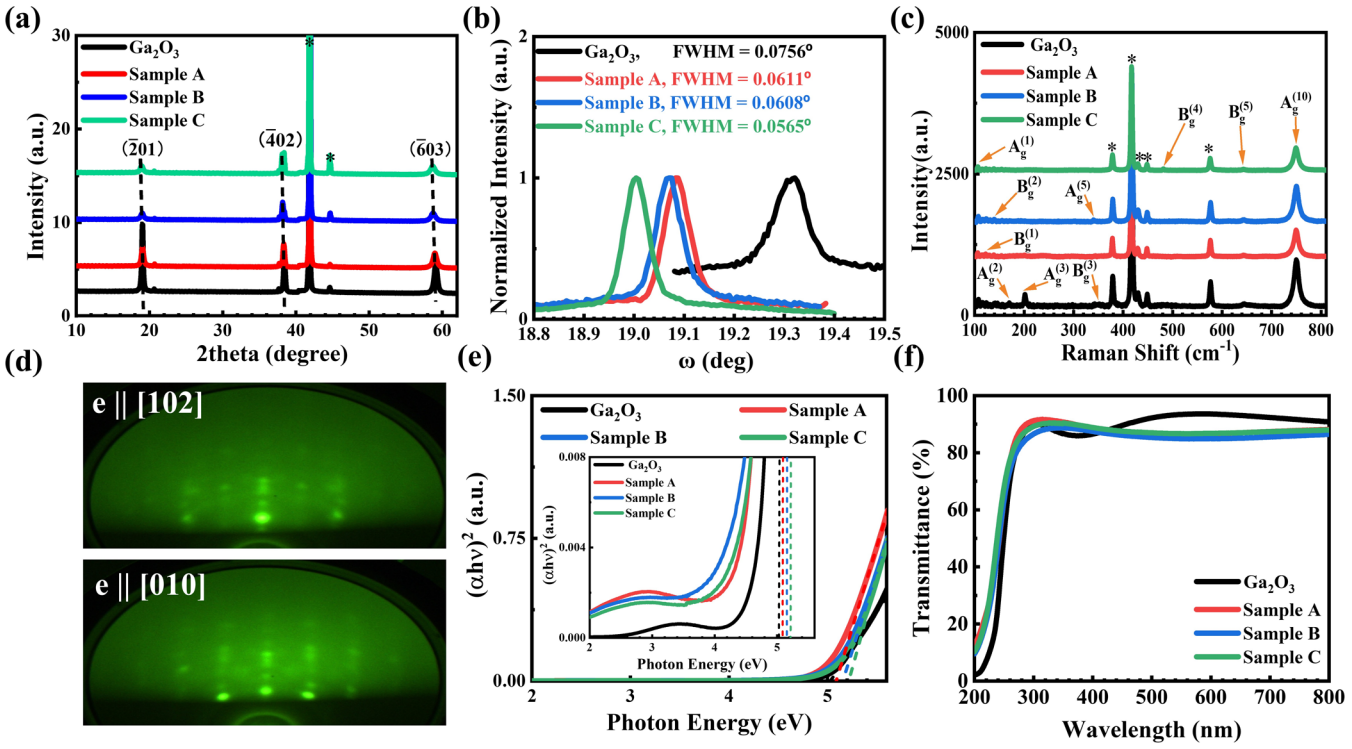

Figure 3. (a) XRD pattern in the $\theta/2\theta$ scan mode, (b) XRD rocking curves, (c) Raman spectra, (d) reflection high-energy electron diffraction (RHEED) patterns of MgGaO sample A, (e) Tauc-plot of the absorption spectra (inset shows absorption peaks between 2 and 4 eV), and (f) transmittance spectra of Ga_2O_3 and samples A, B, and C.

samples and the Ga_2O_3 reference sample indicates that the lattice structure of MgGaO samples could be due to the incorporation of Mg atoms in the lattice structure of Ga_2O_3. Nevertheless, further in-depth Raman studies, along with other characterizations, are necessary to quantify the exact locations of these Mg atoms and strain/relaxation of the films.[40,46]

Reflection high energy electron diffraction (RHEED) was carried out to study the crystallinity of the samples. Figure 3d shows RHEED patterns of the $(\bar{2}01)$ plane of sample A along the [102] and [010] azimuth, which were alternately observed with every 30° rotation in the azimuthal direction. The streaky patterns indicate the single-crystal nature of the film, similar to the RHEED pattern of single-crystal β-Ga_2O_3.[47] Based on the RHEED patterns, the in-plane lattice constants were calculated as ∼3.06 and 5.34 Å, respectively.

Figure 3e shows the Tauc plot of the absorption spectra of Ga_2O_3 and MgGaO samples A, B, and C thin films. The ultrawide-bandgap absorption spectra reaching the UVC region are obtained in all samples. The Tauc equation for semiconductors with direct bandgaps is expressed as follows:[46]

$$(\alpha h\upsilon)^2 = A(h\upsilon - E_g) \quad (1)$$

where α is the absorption coefficient, $h\upsilon$ is energy, and A is a proportionality constant. By extrapolating the linear segment of absorption spectra to intersect the $h\upsilon$-axis with a fitting straight line, the direct bandgap value of the Ga_2O_3 sample is approximately 5.03 eV, which is in good agreement with the reported values.[48,49] It is noted that experimental bandgaps of β-Ga_2O_3 ranging from 4.4 to 5.0 eV at room temperature were reported when absorption or transmittance polarization was employed during the characterization.[50] Bandgaps of MgGaO thin-film samples A, B, and C are 5.09, 5.15, and 5.22 eV, respectively, which increases with an increase in the Mg atomic percent. The inset in Figure 3e shows zoomed in absorption spectra of the samples, indicating a small broad absorption peak at ∼3.4 eV for Ga_2O_3 and at ∼2.6 eV for samples A, B, and C, which is in agreement with the photoresponse around 480 nm, as shown in Figure 5. The transmittance of light of these samples were also measured using the same spectrophotometer. Around 90% transmittance of light was observed across the spectrum for Ga_2O_3 and MgGaO samples A, B and C, as shown in Figure 3f.

A schematic diagram of the β-MgGaO MSM photodetector is illustrated in the inset of Figure 4a. The electrodes are composed of 31 digits of the same size on each side with a length of 475.5 μm, a width of 5 μm, and a spacing of 3 μm; the effective area of the photodetector is 9.1605×10^4 μm^2. Figure 4a−c shows wavelength-dependent $I-V$ characteristics of the MSM devices based on samples A, B, and C under dark conditions and under illumination of 265 and 280 nm light with the same power density of 1.808 mW/cm^2, respectively. For all three devices based on samples A, B, and C, the dark current is around 15 nA, 50 μA, under 265 nm illumination and 100 μA under 280 nm illumination at a bias of 20 V, and photo-to-dark current ratios > 10^3 are obtained for both kinds of illuminations.[51] For the fixed bias, the photocurrent on longer wavelength (280 nm) illumination was larger than that on shorter wavelength (265 nm) illumination. This phenomenon can be ascribed to the different numbers of photogenerated carriers under illumination of different wavelengths but with constant incident power.[52−54] When the film is illuminated with an incident light of a shorter wavelength of 265 nm, fewer photons reach the films, yielding fewer photocarriers, and, in turn, a smaller photocurrent.

Figure 4d−f shows temperature-dependent $I-V$ characteristics of samples A, B, and C under 265 nm UV illumination.

https://doi.org/10.1021/acsaelm.3c00035
ACS Appl. Electron. Mater. 2023, 5, 2122−2130

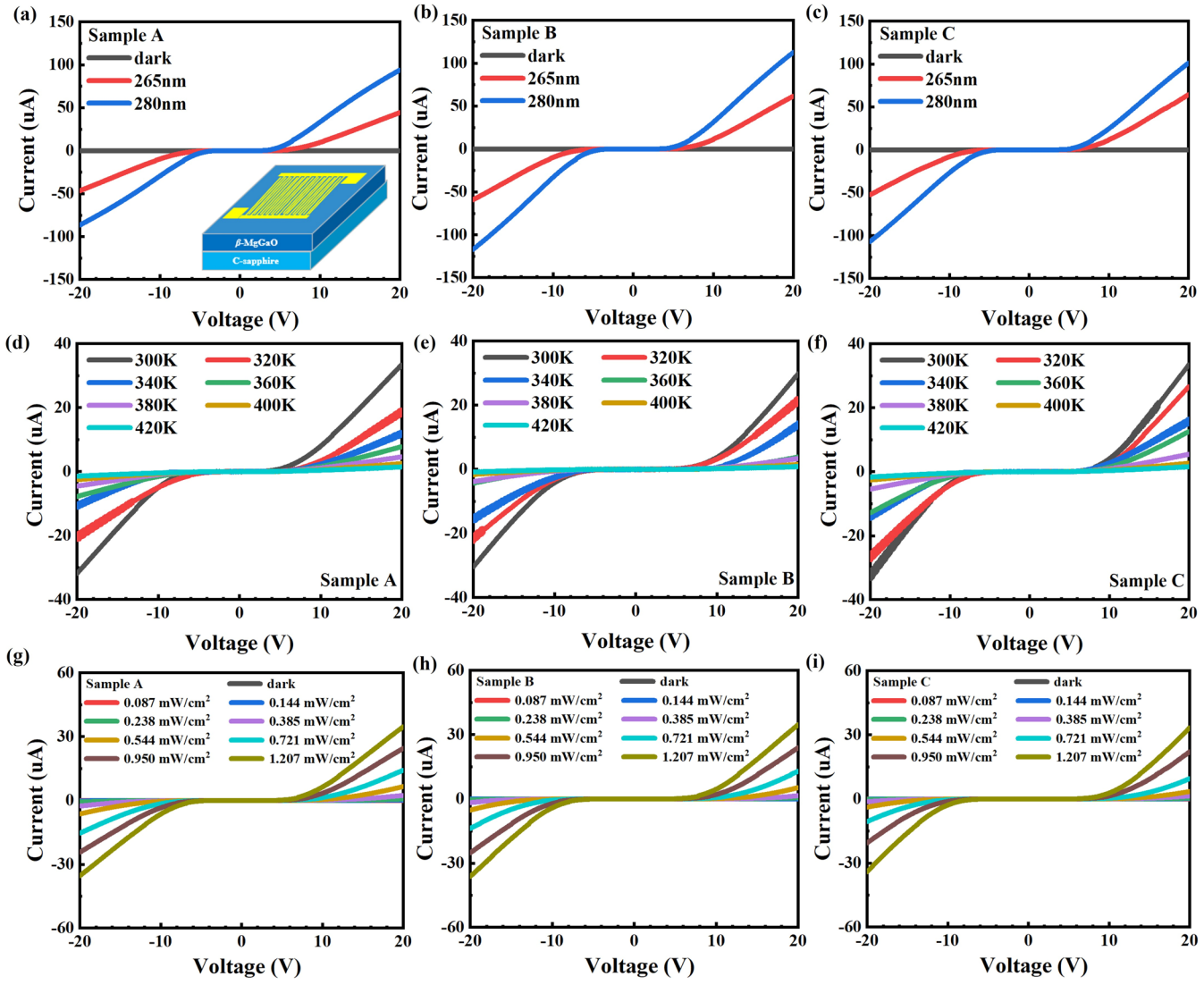

Figure 4. (a)−(c) *I*−*V* characteristics of samples A, B, and C under dark conditions and UV light illumination of 1.808 mW/cm^2. The inset in (a) shows a schematic diagram of the interdigital metal contact structure. (d)−(f) Temperature-dependent *I*−*V* curves of samples A, B, and C under 265 nm illumination. (g)−(i) Power-dependent *I*−*V* curves of samples A, B, and C illuminated by an UV light centered at 265 nm at different light intensities.

The temperature ranges from 300 to 420 K with a step of 20 K. For all samples at a fixed bias (for example, 20 V), the photocurrent decreases with an increase of the temperature. This can be attributed to the enhancement of the nonradiative recombination, mainly in the form of the Shockley−Read−Hall (SRH) recombination, which is a compensating process of carrier generation induced by incident photons.[55] On the one hand, incident photons are absorbed to generate electron−hole pairs, contributing to the photocurrent, and on the other hand, when the temperature increases, electrons in the conduction band and holes in the valence band move to the defect levels and recombine with each other to release phonons, resulting in a decrease of the photocurrent.

Figure 4g−i shows power-dependent *I*−*V* characteristics of the three samples under a 265 nm light source with different power densities ranging from 0.087 to 1.207 mW/cm^2. The generated photocurrent increases with an increase of the incident power density as larger numbers of incident photons are absorbed, generating more photocarriers.

Photocurrent spectra were acquired from MSM device samples A, B, and C under different voltages ranging from 10 to 20 V at wavelengths ranging from 200 to 600 nm. Figure 5a−c shows the results of the three samples, respectively. The photocurrent increases with an increase of the bias for all three samples, indicating the more efficient collection of photocarriers at higher bias. In each sample, two photocurrent peaks are observed. Higher-energy photoresponses are observed at wavelengths of 254, 253, and 247 nm (corresponding to 4.88, 4.90, and 5.02 eV in energy) for samples A, B, and C, respectively. Compared with ∼200 meV larger optical bandgap energies obtained in the absorption experiment in respective samples, these photocurrent peaks may be associated with near-band-edge bound exciton absorption, assuming that the free exciton binding energy in the present MgGaO thin films is close to 0.12 eV, a value attained for β-Ga_2O_3.[56] It is noted that the photocurrent peaks in the UV region for the three samples exhibit symmetric behavior. Similar symmetric photoresponses were also reported in MSM photodetectors based on β-Ga_2O_3 by other groups.[57−59] This phenomenon further strengthens

https://doi.org/10.1021/acsaelm.3c00035
ACS Appl. Electron. Mater. 2023, 5, 2122−2130

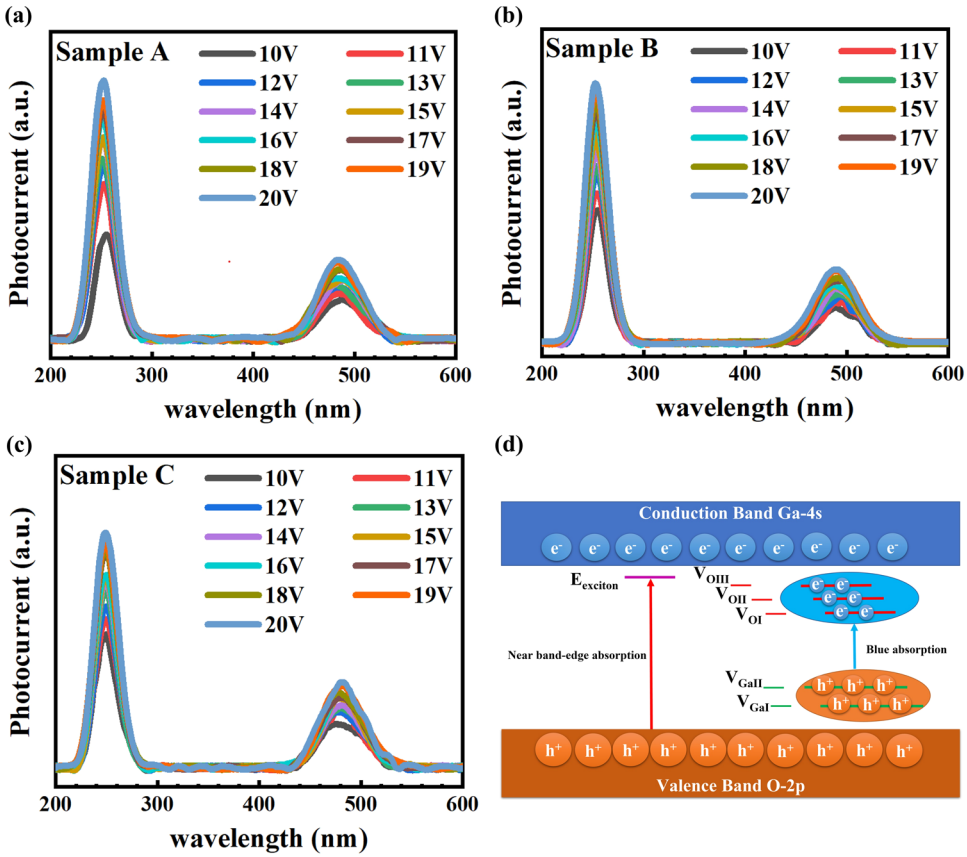

Figure 5. Photocurrent spectra of samples (a) A, (b) B, and (c) C measured under different voltages. (d) Schematic model illustrating the photocurrent mechanism in MgGaO thin films.

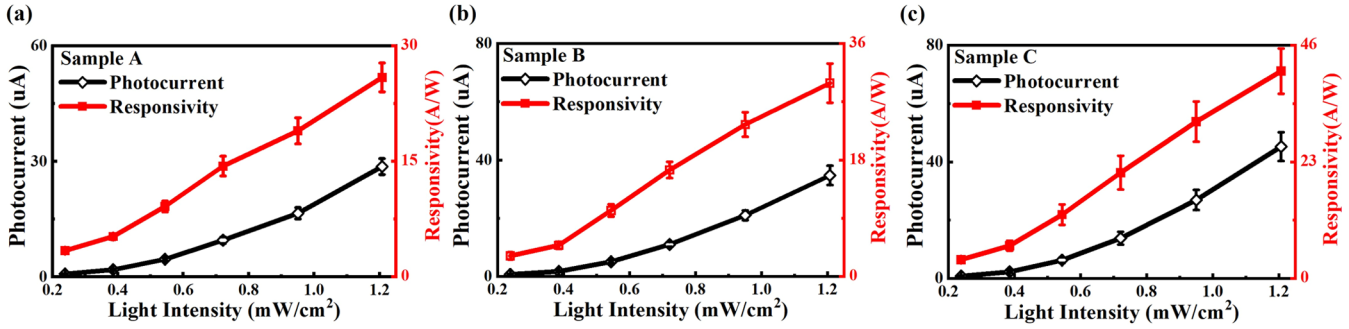

Figure 6. Photocurrent and responsivity versus 265 nm light intensity under 20 V bias for samples (a) A, (b) B, and (c) C, respectively.

the conclusion that the UV photoresponse results from near-band-edge absorption between the relatively flat valence band and narrow "subbands" near the conduction band edge rather than from straight band-to-band transition, which would have been more asymmetric due to the nonlinear density of state function of a conduction band. A lower-energy photoresponse is observed at a wavelength of around 485 nm (corresponding to 2.55 eV in energy) for three samples. The 2.55 eV blue absorption peak may originate from the transition between oxygen vacancy (V_O) energy levels and Ga vacancy (V_{Ga}) energy levels.[60−62] A schematic model illustrating absorption processes contributing to the photocurrent spectra is shown in Figure 5d.

The responsivities of MSM device samples A, B, and C were measured. Figure 6a−c shows the photocurrent and responsivity as a function of 265 nm light intensity for three samples under 20 V bias, respectively. The photocurrent increases with an increase in the light intensity, which is in agreement with Figure 4g−i. The responsivity was calculated based on the following equation:[63]

$$R_\lambda = \frac{I_\lambda - I_d}{P_\lambda S} \tag{2}$$

where I_λ is the photocurrent, I_d is the dark current, P_λ is the incident light intensity, and S is the effective illumination area. As shown in Figure 6a−c, the responsivity increases with an increase in the light intensity. The highest responsivities of samples A, B, and C are 25.9, 29.88, and 40.88 A/W, respectively, at an incident power density of 1.207 mW/cm^2. In contrast, responsivities of 6.89, 0.19, and 0.89 A/W were reported for photodetectors based on semiconductors with

https://doi.org/10.1021/acsaelm.3c00035
ACS Appl. Electron. Mater. 2023, 5, 2122−2130

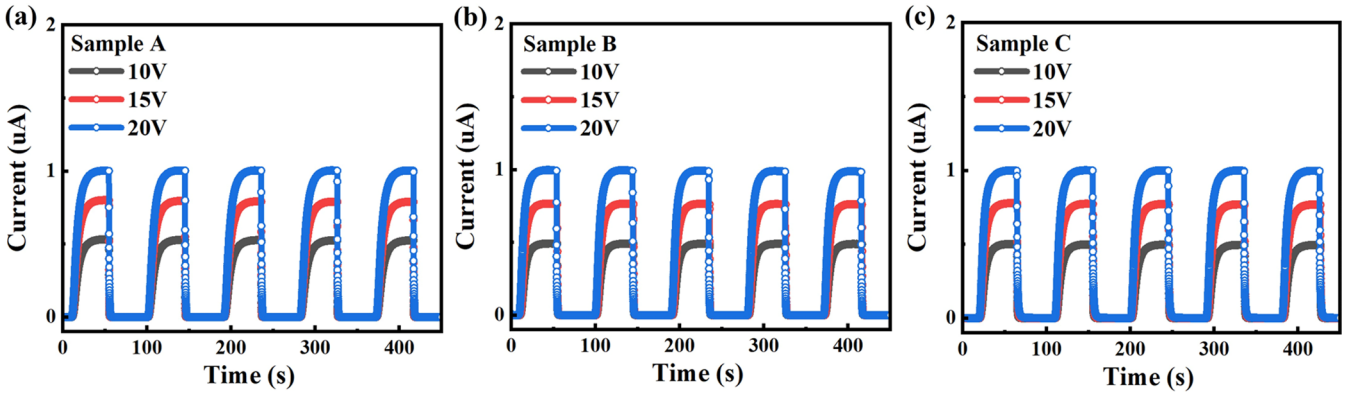

Figure 7. (a)−(c) Normalized $I-t$ characteristics under 0.144 mW/cm^2 265 nm illumination at varying voltages of 10, 15, and 20 V, respectively, for samples A, B, and C.

similar wide bandgaps, i.e., $ZnGa_2O_4$,[64] AlGaN,[65] and $MgGa_2O_4$,[6666] respectively.

Figure 7a−c shows the normalized current−time ($I-t$) dynamics of the photocurrent of MSM device samples A, B, and C, which were measured at biases of 10, 15, and 20 V under 265 nm illumination with a light intensity of 0.144 mW/cm^2. The durations for photocurrent to increase from 0 to $1 - 1/e$ of the steady value and decrease from the steady value to $1/e$ are defined as the rise and decay times, respectively. The rise and decay times of the dynamic change of the photocurrent at a bias of 20 V for samples A, B, and C were statistically calculated to be 6.13 and 0.29 s, 4.85 and 0.29 s, and 4.87 and 0.47 s, respectively. It is noted that a similar rise time of 13 s and decay time of 0.4 s were demonstrated for β-Ga_2O_3 thin-film based photodetectors.[67] The slightly larger decay time of the device for sample C indicates higher quality of the MgGaO film, which is in good agreement with the XRD rocking curves shown in Figure 3b.

4. CONCLUSIONS

UWBG MgGaO thin films were grown by plasma-assisted MBE. Bandgaps of the β-phase MgGaO thin films were engineered from 5.03 to 5.22 eV by incorporating different atomic percentages of Mg^{2+}. The transmittance of all of the samples are around 90%. Based on these MgGaO films, MSM photodetectors with Pt/Au metal contacts were fabricated and characterized. It was shown that the photo-to-dark current ratio is larger than 10^3 at a bias of 20 V. The photocurrent spectra reveal near-band-edge bound exciton absorption and Ga vacancy to oxygen vacancy defect-level transitions, respectively. MgGaO MSM detectors also show very good responsivity and current−time characteristics. This study indicates that UWBG MgGaO semiconductors have a promising potential for deep-UV photodetection applications.

■ ASSOCIATED CONTENT

Supporting Information

The Supporting Information is available free of charge at https://pubs.acs.org/doi/10.1021/acsaelm.3c00035.

MBE growth conditions and film parameters of β-phase Ga_2O_3 and MgGaO samples; Raman peaks of all samples; illustration of the MgGaO monoclinic structure (PDF)

■ AUTHOR INFORMATION

Corresponding Author

Jianlin Liu − *Department of Electrical and Computer Engineering, University of California, Riverside, Riverside, California 92521, United States;* orcid.org/0000-0001-6513-0867; Phone: 1-9518277131; Email: jianlin@ece.ucr.edu; Fax: 1-9518272425

Authors

Tianchen Yang − *Department of Electrical and Computer Engineering, University of California, Riverside, Riverside, California 92521, United States*

Chengyun Shou − *Department of Electrical and Computer Engineering, University of California, Riverside, Riverside, California 92521, United States*

Long Xu − *Department of Electrical and Computer Engineering, University of California, Riverside, Riverside, California 92521, United States; School of Physical Science and Technology, Southwest University, Chongqing 400715, China;* orcid.org/0000-0002-3243-4087

Jason Tran − *Department of Physics and Astronomy, University of California, Riverside, Riverside, California 92521, United States*

Yanwei He − *Department of Electrical and Computer Engineering, University of California, Riverside, Riverside, California 92521, United States*

Yuan Li − *Department of Electrical and Computer Engineering, University of California, Riverside, Riverside, California 92521, United States*

Peng Wei − *Department of Physics and Astronomy, University of California, Riverside, Riverside, California 92521, United States;* orcid.org/0000-0003-2289-6007

Complete contact information is available at: https://pubs.acs.org/10.1021/acsaelm.3c00035

Author Contributions

T.Y.: conceptualization, methodology, software, validation, formal analysis, investigation, writing−original draft, writing—review & editing, resources, data curation, and project administration. C.S.: resources, validation, software, and writing—review & editing. L.X.: methodology and resources. J.T.: validation and resources. Y.H.: methodology and resources. Y.L.: software and resources. P.W.: resources. J.L.: conceptualization, methodology, resources, project administration, supervision, funding acquisition, manuscript writing, review and editing.

https://doi.org/10.1021/acsaelm.3c00035
ACS Appl. Electron. Mater. 2023, 5, 2122−2130

Funding

This work was supported by the National Science Foundation (ECCS-2105566).

Notes

The authors declare no competing financial interest.

■ ACKNOWLEDGMENTS

The authors acknowledge the use of facilities and instrumentation at the UC Irvine Materials Research Institute (IMRI), which is supported in part by the National Science Foundation through the UC Irvine Materials Research Science and Engineering Center (DMR-2011967). The authors acknowledge the use of the XPS instrument at UC Riverside, which is supported by the National Science Foundation (DMR-0958796). J.T. and P.W. would like to acknowledge NSF under award NSF CAREER-2046648.

■ REFERENCES

(1) Tran, N. H.; Le, B. H.; Zhao, S.; Mi, Z. On the Mechanism of Highly Efficient P-Type Conduction of Mg-Doped Ultra-Wide-Bandgap AlN Nanostructures. *Appl. Phys. Lett.* **2017**, *110*, No. 032102.

(2) Kim, M.; Seo, J.-H.; Singisetti, U.; Ma, Z. Recent Advances in Free-Standing Single Crystalline Wide Band-Gap Semiconductors and Their Applications: GaN, SiC, ZnO, β-Ga_2O_3, and Diamond. *J. Mater. Chem. C* **2017**, *5*, 8338−8354.

(3) Xie, C.; Lu, X.-T.; Tong, X.-W.; Zhang, Z.-X.; Liang, F.-X.; Liang, L.; Luo, L.-B.; Wu, Y.-C. Recent Progress in Solar-Blind Deep-Ultraviolet Photodetectors Based on Inorganic Ultrawide Bandgap Semiconductors. *Adv. Funct. Mater.* **2019**, *29*, No. 1806006.

(4) Tsao, J. Y.; Chowdhury, S.; Hollis, M. A.; Jena, D.; Johnson, N. M.; Jones, K. A.; Kaplar, R. J.; Rajan, S.; Van de Walle, C. G.; Bellotti, E.; Chua, C. L.; Collazo, R.; Coltrin, M. E.; Cooper, J. A.; Evans, K. R.; Graham, S.; Grotjohn, T. A.; Heller, E. R.; Higashiwaki, M.; Islam, M. S.; Juodawlkis, P. W.; Khan, M. A.; Koehler, A. D.; Leach, J. H.; Mishra, U. K.; Nemanich, R. J.; Pilawa-Podgurski, R. C. N.; Shealy, J. B.; Sitar, Z.; Tadjer, M. J.; Witulski, A. F.; Wraback, M.; Simmons, J. A. Ultrawide-Bandgap Semiconductors: Research Opportunities and Challenges. *Adv. Electron. Mater.* **2018**, *4*, No. 1600501.

(5) Monroy, E.; Omn s, F.; Calle, F. Wide-Bandgap Semiconductor Ultraviolet Photodetectors. *Semicond. Sci. Technol.* **2003**, *18*, R33−R51.

(6) Pearton, S. J.; Yang, J.; Cary, P. H.; Ren, F.; Kim, J.; Tadjer, M. J.; Mastro, M. A. A Review of Ga_2O_3 Materials, Processing, and Devices. *Appl. Phys. Rev.* **2018**, *5*, No. 011301.

(7) Xia, X.; Chen, Y.; Feng, Q.; Liang, H.; Tao, P.; Xu, M.; Du, G. Hexagonal Phase-Pure Wide Band Gap ε-Ga_2O_3 Films Grown on 6H-SiC Substrates by Metal Organic Chemical Vapor Deposition. *Appl. Phys. Lett.* **2016**, *108*, No. 202103.

(8) Rafique, S.; Han, L.; Zhao, H. Synthesis of Wide Bandgap Ga_2O_3 (E_g ∼ 4.6−4.7 EV) Thin Films on Sapphire by Low Pressure Chemical Vapor Deposition. *Phys. Status Solidi A* **2016**, *213*, 1002−1009.

(9) Sharma, S.; Zeng, K.; Saha, S.; Singisetti, U. Field-Plated Lateral Ga_2O_3 MOSFETs With Polymer Passivation and 8.03 kV Breakdown Voltage. *IEEE Electron Device Lett.* **2020**, *41*, 836−839.

(10) Zeng, K.; Vaidya, A.; Singisetti, U. 1.85 kV Breakdown Voltage in Lateral Field-Plated Ga_2O_3 MOSFETs. *IEEE Electron Device Lett.* **2018**, *39*, 1385−1388.

(11) Yang, J.; Ahn, S.; Ren, F.; Pearton, S. J.; Jang, S.; Kuramata, A. High Breakdown Voltage (−201) β-Ga_2O_3 Schottky Rectifiers. *IEEE Electron Device Lett.* **2017**, *38*, 906−909.

(12) Zhao, B.; Wang, F.; Chen, H.; Zheng, L.; Su, L.; Zhao, D.; Fang, X. An Ultrahigh Responsivity (9.7 mA W^{-1}) Self-Powered Solar-Blind Photodetector Based on Individual ZnO−Ga_2O_3 Heterostructures. *Adv. Funct. Mater.* **2017**, *27*, No. 1700264.

(13) Kumar, A.; Bag, A. Ultra-High Responsivity (>12.34 kA W −1) of Ga−In Bimetallic Oxide Nanowires Based Deep-UV Photodetector. *Nanotechnology* **2020**, *31*, No. 304001.

(14) Qin, Y.; Li, L.; Zhao, X.; Tompa, G. S.; Dong, H.; Jian, G.; He, Q.; Tan, P.; Hou, X.; Zhang, Z.; Yu, S.; Sun, H.; Xu, G.; Miao, X.; Xue, K.; Long, S.; Liu, M. Metal−Semiconductor−Metal ε-Ga_2O_3 Solar-Blind Photodetectors with a Record-High Responsivity Rejection Ratio and Their Gain Mechanism. *ACS Photonics* **2020**, *7*, 812−820.

(15) Oh, S.; Kim, C.-K.; Kim, J. High Responsivity β-Ga_2O_3 Metal−Semiconductor−Metal Solar-Blind Photodetectors with Ultraviolet Transparent Graphene Electrodes. *ACS Photonics* **2018**, *5*, 1123−1128.

(16) Baldini, M.; Albrecht, M.; Fiedler, A.; Irmscher, K.; Schewski, R.; Wagner, G. Editors' Choice-Si- and Sn-Doped Homoepitaxial β-Ga_2O_3 Layers Grown by MOVPE on (010)-Oriented Substrates. *ECS J. Solid State Sci. Technol.* **2017**, *6*, Q3040−Q3044.

(17) Kalarickal, N. K.; Xia, Z.; McGlone, J.; Krishnamoorthy, S.; Moore, W.; Brenner, M.; Arehart, A. R.; Ringel, S. A.; Rajan, S. Mechanism of Si Doping in Plasma Assisted MBE Growth of β-Ga_2O_3. *Appl. Phys. Lett.* **2019**, *115*, No. 152106.

(18) Suzuki, N.; Ohira, S.; Tanaka, M.; Sugawara, T.; Nakajima, K.; Shishido, T. Fabrication and Characterization of Transparent Conductive Sn-Doped β-Ga_2O_3 Single Crystal. *Phys. Status Solidi C* **2007**, *4*, 2310−2313.

(19) Ahmadi, E.; Koksaldi, O. S.; Kaun, S. W.; Oshima, Y.; Short, D. B.; Mishra, U. K.; Speck, J. S. Ge Doping of β-Ga_2O_3 Films Grown by Plasma-Assisted Molecular Beam Epitaxy. *Appl. Phys. Express* **2017**, *10*, No. 041102.

(20) Moser, N.; McCandless, J.; Crespo, A.; Leedy, K.; Green, A.; Neal, A.; Mou, S.; Ahmadi, E.; Speck, J.; Chabak, K.; Peixoto, N.; Jessen, G. Ge-Doped β-Ga_2O_3 MOSFETs. *IEEE Electron Device Lett.* **2017**, *38*, 775−778.

(21) Farzana, E.; Mauze, A.; Varley, J. B.; Blue, T. E.; Speck, J. S.; Arehart, A. R.; Ringel, S. A. Influence of Neutron Irradiation on Deep Levels in Ge-Doped (010) β-Ga_2O_3 Layers Grown by Plasma-Assisted Molecular Beam Epitaxy. *APL Mater.* **2019**, *7*, No. 121102.

(22) Yan, J.; Qu, C. Electronic Structure and Optical Properties of F-Doped β-Ga_2O_3 from First Principles Calculations. *J. Semicond.* **2016**, *37*, No. 042002.

(23) Wang, Y.; Su, J.; Yuan, H.; Lin, Z.; Zhang, J.; Hao, Y.; Chang, J. Impurity Level Properties in Transition Metal Doped α-Ga_2O_3 for Optoelectronic Applications. *Semicond. Sci. Technol.* **2021**, *36*, No. 095026.

(24) Chen, Y.; Lu, Y.; Yang, X.; Li, S.; Li, K.; Chen, X.; Xu, Z.; Zang, J.; Shan, C. Bandgap Engineering of Gallium Oxides by Crystalline Disorder. *Mater. Today Phys.* **2021**, *18*, No. 100369.

(25) Kyrtsos, A.; Matsubara, M.; Bellotti, E. On the Feasibility of P-Type Ga_2O_3. *Appl. Phys. Lett.* **2018**, *112*, No. 032108.

(26) Wong, M. H.; Lin, C.-H.; Kuramata, A.; Yamakoshi, S.; Murakami, H.; Kumagai, Y.; Higashiwaki, M. Acceptor Doping of β-Ga_2O_3 by Mg and N Ion Implantations. *Appl. Phys. Lett.* **2018**, *113*, No. 102103.

(27) Qian, Y. P.; Guo, D. Y.; Chu, X. L.; Shi, H. Z.; Zhu, W. K.; Wang, K.; Huang, X. K.; Wang, H.; Wang, S. L.; Li, P. G.; Zhang, X. H.; Tang, W. H. Mg-Doped p-Type β- Ga_2O_3 Thin Film for Solar-Blind Ultraviolet Photodetector. *Mater. Lett.* **2017**, *209*, 558−561.

(28) Alema, F.; Hertog, B.; Ledyaev, O.; Volovik, D.; Thoma, G.; Miller, R.; Osinsky, A.; Mukhopadhyay, P.; Bakhshi, S.; Ali, H.; Schoenfeld, W. V. Solar Blind Photodetector Based on Epitaxial Zinc Doped Ga_2O_3 Thin Film. *Phys. Status Solidi A* **2017**, *214*, No. 1600688.

(29) Li, L.; Liao, F.; Hu, X. The Possibility of N−P Codoping to Realize P Type β-Ga_2O_3. *Superlattices Microstruct.* **2020**, *141*, No. 106502.

(30) Galazka, Z. β- Ga_2O_3 for Wide-Bandgap Electronics and Optoelectronics. *Semicond. Sci. Technol.* **2018**, *33*, No. 113001.

https://doi.org/10.1021/acsaelm.3c00035
ACS Appl. Electron. Mater. 2023, 5, 2122−2130

(31) Miller, R.; Alema, F.; Osinsky, A. Epitaxial β-Ga_2O_3 and β-$(Al_xGa_{1-x})_2O_3$/ β-Ga_2O_3 Heterostructures Growth for Power Electronics. *IEEE Trans. Semicond. Manuf.* **2018**, *31*, 467−474.
(32) Bhuiyan, A. F. M. A. U.; Feng, Z.; Johnson, J. M.; Huang, H.-L.; Hwang, J.; Zhao, H. MOCVD Growth of β-Phase $(Al_xGa_{1-x})_2O_3$ on $(\bar{2}01)$ β-Ga_2O_3 Substrates. *Appl. Phys. Lett.* **2020**, *117*, No. 142107.
(33) Hu, W.; Li, S.; Hu, Y.; Wan, L.; Jiao, S.; Hu, W.; Talwar, D. N.; Feng, Z. C.; Li, T.; Xu, J.; Wei, L.; Guo, W. Optical and Electronic Properties of $(Al_xGa_{1-x})_2O_3/Al_2O_3$ (X>0.4) Films Grown by Magnetron Sputtering. *J. Alloys Compd.* **2021**, *864*, No. 158765.
(34) Shen, Y.-S.; Wang, W.-K.; Horng, R.-H. Characterizations of Metal-Oxide-Semiconductor Field-Effect Transistors of ZnGaO Grown on Sapphire Substrate. *IEEE J. Electron Devices Soc.* **2017**, *5*, 112−116.
(35) Wang, L.; Han, X. ZnGaO Thin Film of Transparent Oxide Materials By Pulse Laser Deposition. In *Advanced Solid State Lasers*; Optica Publishing Group, 2019.
(36) Dong, M.; Zheng, W.; Xu, C.; Lin, R.; Zhang, D.; Zhang, Z.; Huang, F. Ultrawide-Bandgap Amorphous MgGaO: Nonequilibrium Growth and Vacuum Ultraviolet Application. *Adv. Opt. Mater.* **2019**, *7*, No. 1801272.
(37) Xu, C.; Du, Z.; Huang, Y.; Dong, M.; Lin, R.; Li, Y.; Wang, B.; Zheng, W.; Huang, F. Correction to "Amorphous-MgGaO Film Combined with Graphene for Vacuum-Ultraviolet Photovoltaic Detector". *ACS Appl. Mater. Interfaces* **2019**, *11*, 9641.
(38) Bi, X.; Wu, Z.; Huang, Y.; Tang, W. Stabilization and Enhanced Energy Gap by Mg Doping in ε-Phase Ga_2O_3 Thin Films. *AIP Adv.* **2018**, *8*, No. 025008.
(39) Rafique, S.; Han, L.; Zhao, H. (Invited) Ultrawide Bandgap β-Ga_2O_3 Thin Films: Growths, Properties and Devices. *ECS Trans.* **2017**, *80*, 203.
(40) Onuma, T.; Fujioka, S.; Yamaguchi, T.; Itoh, Y.; Higashiwaki, M.; Sasaki, K.; Masui, T.; Honda, T. Polarized Raman Spectra in β-Ga_2O_3 Single Crystals. *J. Cryst. Growth* **2014**, *401*, 330−333.
(41) Kranert, C.; Sturm, C.; Schmidt-Grund, R.; Grundmann, M. Raman Tensor Elements of β-Ga_2O_3. *Sci. Rep.* **2016**, *6*, No. 35964.
(42) Wungu, T. D. K.; Sakaue, M.; Aspera, S. M.; Thuy, T. L. P.; Alaydrus, M.; Kasai, H.; Ishihara, T. First Principles Study on the Electronic Structure and Properties of Sr- and Mg-Doped $LaGaO_3$. *ECS Trans.* **2013**, *57*, 2715−2722.
(43) Geller, S. Crystal Structure of β-Ga_2O_3. *J. Chem. Phys.* **1960**, *33*, 676−684.
(44) Zhang, Z.; Ding, Z.; Guo, X.; Luo, Z.; Wei, J.; Yang, C.; Huang, Y.; Li, Z. First-Principle Calculations of Electronic and Optical Properties of Ti-Doped β-Ga_2O_3 with Intrinsic Defects. *Mater. Res. Express* **2019**, *6*, No. 105920.
(45) Ma, X.; Zhang, Y.; Dong, L.; Jia, R. First-Principles Calculations of Electronic and Optical Properties of Aluminum-Doped β-Ga_2O_3 with Intrinsic Defects. *Results Phys.* **2017**, *7*, 1582−1589.
(46) Zhang, K.; Xu, Z.; Zhang, S.; Wang, H.; Cheng, H.; Hao, J.; Wu, J.; Fang, F. Raman and Photoluminescence Properties of Un-/Ion-Doped β-Ga_2O_3 Single-Crystals Prepared by Edge-Defined Film-Fed Growth Method. *Phys. B* **2021**, *600*, No. 412624.
(47) Wei, J.; Kim, K.; Liu, F.; Wang, P.; Zheng, X.; Chen, Z.; Wang, D.; Imran, A.; Rong, X.; Yang, X.; Xu, F.; Yang, J.; Shen, B.; Wang, X. β-Ga_2O_3 Thin Film Grown on Sapphire Substrate by Plasma-Assisted Molecular Beam Epitaxy. *J. Semicond.* **2019**, *40*, No. 012802.
(48) Chen, Z.; Ge, K.; Meng, D.; Chen, X. Pure-Phase Ga_2O_3 Films Were Deposited on Sapphire Substrates by Radio Frequency Magnetron Sputtering. *Mater. Lett.* **2022**, *320*, No. 132385.
(49) Oshima, T.; Okuno, T.; Fujita, S. Ga_2O_3 Thin Film Growth on C-Plane Sapphire Substrates by Molecular Beam Epitaxy for Deep-Ultraviolet Photodetectors. *Jpn. J. Appl. Phys.* **2007**, *46*, 7217.
(50) Onuma, T.; Saito, S.; Sasaki, K.; Masui, T.; Yamaguchi, T.; Honda, T.; Higashiwaki, M. Valence Band Ordering in β-Ga_2O_3 Studied by Polarized Transmittance and Reflectance Spectroscopy. *Jpn. J. Appl. Phys.* **2015**, *54*, No. 112601.
(51) Singh Pratiyush, A.; Krishnamoorthy, S.; Vishnu Solanke, S.; Xia, Z.; Muralidharan, R.; Rajan, S.; Nath, D. N. High Responsivity in Molecular Beam Epitaxy Grown β- Ga_2O_3 Metal Semiconductor Metal Solar Blind Deep-UV Photodetector. *Appl. Phys. Lett.* **2017**, *110*, No. 221107.
(52) Yao, J.; Deng, Z.; Zheng, Z.; Yang, G. Stable, Fast UV−Vis−NIR Photodetector with Excellent Responsivity, Detectivity, and Sensitivity Based on α-In_2Te_3 Films with a Direct Bandgap. *ACS Appl. Mater. Interfaces* **2016**, *8*, 20872−20879.
(53) Yao, J. D.; Shao, J. M.; Yang, G. W. Ultra-Broadband and High-Responsive Photodetectors Based on Bismuth Film at Room Temperature. *Sci. Rep.* **2015**, *5*, No. 12320.
(54) Chang, C.; Cheng, H.-H.; Sevison, G. A.; Hendrickson, J. R.; Li, Z.; Agha, I.; Mathews, J.; Soref, R. A.; Sun, G. Power-Dependent Investigation of Photo-Response from GeSn-Based p-i-n Photodetector Operating at High Power Density. *Materials* **2022**, *15*, 989.
(55) Ishitani, Y. Temperature Dependence of Recombination Processes of Photogenerated Carriers in a Quantum-Well Structure. *J. Appl. Phys.* **1999**, *86*, 6816−6821.
(56) Yamaoka, S.; Mikuni, Y.; Nakayama, M. Characteristics of Multi-Photon Absorption in a β-Ga_2O_3 Single Crystal. *J. Phys. Soc. Jpn.* **2019**, *88*, No. 113701.
(57) Pratiyush, A. S.; Krishnamoorthy, S.; Solanke, S. V.; Xia, Z.; Muralidharan, R.; Rajan, S.; Nath, D. N. High Responsivity in Molecular Beam Epitaxy (MBE) Grown β-Ga_2O_3 Metal Semiconductor Metal (MSM) Solar Blind Deep- UV Photodetector. *Appl. Phys. Lett.* **2017**, *110*, No. 221107.
(58) *Review of Deep Ultraviolet Photodetector Based on Gallium Oxide-IOPscience*. https://iopscience.iop.org/article/10.1088/1674-1056/28/1/018501/meta (accessed February 18, 2023).
(59) Feng, Q.; Huang, L.; Han, G.; Li, F.; Li, X.; Fang, L.; Xing, X.; Zhang, J.; Mu, W.; Jia, Z.; Guo, D.; Tang, W.; Tao, X.; Hao, Y. Comparison Study of β-Ga_2O_3 Photodetectors on Bulk Substrate and Sapphire. *IEEE Trans. Electron Devices* **2016**, *63*, 3578−3583.
(60) Zhu, X.; Zhang, Y.-W.; Zhang, S.-N.; Huo, X.-Q.; Zhang, X.-H.; Li, Z.-Q. Defect Energy Levels in Monoclinic β-Ga_2O_3. *J. Lumin.* **2022**, *246*, No. 118801.
(61) Mi, W.; Luan, C.; Li, Z.; Zhao, C.; Feng, X.; Ma, J. Ultraviolet−Green Photoluminescence of β-Ga_2O_3 Films Deposited on $MgAl_6O_{10}$ (100) Substrate. *Opt. Mater.* **2013**, *35*, 2624−2628.
(62) Zhang, K.; Xu, Z.; Zhao, J.; Wang, H.; Hao, J.; Zhang, S.; Cheng, H.; Dong, B. Temperature-Dependent Raman and Photoluminescence of β-Ga_2O_3 Doped with Shallow Donors and Deep Acceptors Impurities. *J. Alloys Compd.* **2021**, *881*, No. 160665.
(63) Qin, Y.; Long, S.; Dong, H.; He, Q.; Jian, G.; Zhang, Y.; Hou, X.; Tan, P.; Zhang, Z.; Lv, H.; Liu, Q.; Liu, M. Review of Deep Ultraviolet Photodetector Based on Gallium Oxide. *Chin. Phys. B* **2019**, *28*, No. 018501.
(64) Ling, K.; Li, K.; Bai, R.; Zhao, B.; Liu, X. Fabrication and Performance Characterization of Deep UV Photodetectors Based on Magnetron Sputtered $ZnGa_2O_4$ Thin Films. *Mater. Sci. Semicond. Process.* **2022**, *152*, No. 107096.
(65) Xie, F.; Xie, F.; Xie, F.; Gu, Y.; Gu, Y.; Hu, Z.; Yu, B.; Yang, G.; Yang, G. Ultra-Low Dark Current Back-Illuminated AlGaN-Based Solar-Blind Ultraviolet Photodetectors with Broad Spectral Response. *Opt. Express* **2022**, *30*, 23756−23762.
(66) Hou, Q.; Liu, K.; Chen, X.; Yang, J.; Ai, Q.; Cheng, Z.; Zhu, Y.; Li, B.; Liu, L.; Shen, D. Effects of Mg Component Ratio on Photodetection Performance of $MgGa_2O_4$ Solar-Blind Ultraviolet Photodetectors. *Phys. Status Solidi RRL* **2022**, *16*, No. 2200137.
(67) Liu, X. Z.; Guo, P.; Sheng, T.; Qian, L. X.; Zhang, W. L.; Li, Y. R. β-Ga_2O_3 Thin Films on Sapphire Pre-Seeded by Homo-Self-Templated Buffer Layer for Solar-Blind UV Photodetector. *Opt. Mater.* **2016**, *51*, 203−207.

https://doi.org/10.1021/acsaelm.3c00035
ACS Appl. Electron. Mater. 2023, 5, 2122−2130